

An efficient local operator based Q-RTM algorithm with multi-stage optimization

Tong Zhou[†], Wenyi Hu^{*} and Jieyuan Ning[†]

^{*}*Advanced Geophysical Technology Inc., Houston, Texas, USA*

Email: wenyi.hu@agtgeo.com

[†]*ITAG Institute of Theoretical and Applied Geophysics, School of Earth and Space Sciences, Peking University, Beijing, China*

(November 16, 2017)

Reversion manuscript v1.3

Running head: **Finite-Difference Q-RTM**

ABSTRACT

Most existing Q-compensated reverse time migration (Q-RTM) algorithms are based on pseudo-spectral methods. Because of the global nature of pseudo-spectral operators, these methods are not ideal for efficient parallelization, implying that they may suffer from high computational cost and inefficient memory usage for large scale industrial problems. In this work, we report a novel Q-RTM algorithm - the multi-stage optimized Q-RTM method. This Q-RTM algorithm employs a finite-difference method to compensate both the amplitude and the phase simultaneously by uniquely combining two techniques: 1) negative τ method for the amplitude compensation; 2) a multi-stage dispersion optimization technique for the phase correction. To prevent high frequency noise from growing exponentially and ruining the imaging results, we apply a finite impulse response (FIR) low-pass filter using the Kaiser Window. Both the theoretical analyses and numerical experiments demonstrate that

this Q-RTM algorithm precisely recovers the decayed amplitude and corrects the distorted phase caused by seismic attenuation effects, and hence produces higher resolution subsurface images with the correct structural depth information. This new method performs best in the frequency range of 10 Hz - 70 Hz. Compared to the pseudo-spectral Q-RTM methods, this Q-RTM approach offers nearly identical imaging quality. Based on local numerical differential operators, this Q-RTM method is very suitable for parallel computing and GPU implementation, an important feature for large 3D seismic surveys.

INTRODUCTION

A seismic wave loses energy when it travels through viscoelastic regions, such as fluid-saturated reservoirs, gas chimneys, or gas clouds (Muller et al., 2010), causing amplitude decay, phase change, wavelet distortion, travel time change, and high frequency component loss (Kjartansson, 1979; Blanch et al., 1995; Hu et al., 2011, 2016) in seismic data. If these seismic data are processed using conventional seismic processing tools, the imaging quality will be degraded, observed as illumination dim, depth shift, and resolution reduction (Yu et al., 2002; Zhou et al., 2011). Therefore, when attenuation is strong, it is necessary to compensate the attenuation effects accurately in seismic imaging processes.

To improve the imaging quality when lossy regions are present, researchers have developed many Q-compensation approaches for various imaging methods. Inverse Q filtering technology was widely used in early days (Bickel and Natarajan, 1985; Hargreaves, 1991). However, because inverse Q filtering is essentially a space-variant or a time-variant filter applied on data prior to migration, this approach is inappropriate for long offsets due to the event separation difficulty and inaccuracy for strong Q heterogeneity scenarios. Like other Q-compensation methods, inverse Q filtering methods are also unstable in the presence of noise. A prestack Kirchhoff Q-migration method compensates the attenuation effects in a more accurate way by honoring energy absorption effects along the 3D raypath for each trace to be migrated, thus improving the amplitude-versus-offset (AVO) attributes (Traynin et al., 2008). However, the Kirchhoff migration method has some limitations. The high frequency assumption in a Kirchhoff migration is no longer valid in the velocity models with sharp boundaries and in complex geological structures causing multi-pathing issues. On the other hand, one-way wave equation migration (WEM) can handle more geologically real-

istic velocity models and a Q-compensation procedure can easily be incorporated because one-way wave equation method is implemented in the frequency domain (Dai and West, 1994; Yu et al., 2002). Nevertheless, the WEM is inaccurate when there are strong lateral heterogeneities and when there is multi-pathing involved.

Reverse time migration (RTM) (Baysal et al., 1983) is regarded as an advanced seismic imaging technology for complex geological structures (Etgen et al., 2009), because it features a full wave propagation engine to simulate the full range of seismic wave phenomena. Although RTM has become a standard seismic processing technology, there has not been much research effort being directed toward the Q-compensated RTM (Q-RTM), partially because of lacking reliable Q models. With the development of ray-based Q-tomography methods (Clark et al., 2009; Xin et al., 2010; Hu et al., 2011; Cavalca et al., 2011) and wave equation based Q-tomography methods (Shen et al., 2014; Shen and Zhu, 2015; Dutta, 2016; Dutta and Schuster, 2016) in recent years, the Q model building technology becomes more and more practical, which paves the way for high fidelity seismic imaging below low-Q or high attenuation zones. The main remaining obstacle to Q-RTM research is that a practical and efficient time-domain Q-compensated wave propagation modeling algorithm was not well established (Zhu et al., 2014). A successful Q-compensated wave propagation process boosts the amplitude accurately while maintaining the same dispersion relation as the Q-attenuation process. Several Q-RTM algorithms were proposed to simulate this wave behavior by decoupling the attenuation effects on the amplitude and the phase by modifying the governing equations of wave propagation (Zhang et al., 2010; Zhu et al., 2014; Xie et al., 2015). These algorithms compensate the Q effects properly and improve the migration image qualities, but they are all based on the Kjartansson's constant Q (KCQ) model and pseudo-spectral methods. In such a method, global numerical differential operators

are employed to evaluate the spatial derivatives. This category of Q-RTM algorithms is not suitable for industrial sized projects because the Fourier pseudo-spectral methods are computationally intensive and hard to parallelize for large 3D studies (Ayala and Wang, 2013). As a result, pseudo-spectral based Q-RTM methods are not widely employed in the oil/gas industry. From a computational efficiency perspective, local operators are preferable than global operators (Li et al., 2006; Abubakar et al., 2008, 2009, 2011). There are also many attempts made to develop finite-difference Q-compensated wave propagation engines (Causse and Ursin, 2000; Deng and McMechan, 2007, 2008; Bai et al., 2013). However, these methods can only recover the amplitudes without precisely controlling the phase. Guo et al. (2016) concluded that the simple back-propagator based on the GSLS model cannot correct the phase distortion. Another category is the visco-acoustic least square reverse time migration (Q-LSRTM), which takes visco-acoustic effects into account in conventional LSRTM methods (Dutta and Schuster, 2014; Dai et al., 2015; Sun et al., 2015a, 2016). Generally, LSRTM can improve the image resolution and can produce more accurate images than conventional migration methods but its computational cost is very high.

In this work, we develop a novel Q-RTM algorithm based on finite-difference operators. Because finite-difference is a local numerical differential operator, the Q-RTM algorithm is very efficient and suitable for parallelization on GPUs. The main challenge of this Q-RTM algorithm is to compensate the amplitude and the phase simultaneously while maintaining the system's stability. To overcome this difficulty, we propose a new finite-difference Q-compensated wave propagation engine which includes two unique techniques. One is the negative- τ method to compensate the amplitude without sacrificing the stability. The other technique is the multi-stage optimization scheme for accurate phase recovery. Numerical examples show that this algorithm can compensate both the amplitude loss and the phase

distortion precisely and efficiently. Furthermore, this Q-RTM method is very suitable for fine-grained parallel computing, and it can be incorporated into the currently existing finite-difference based conventional RTM code straightforwardly with minimum code structure modification.

METHODOLOGY

Theory of RTM and Q-RTM

In a conventional RTM process without considering attenuation effects, the forward-propagated wavefield $S(\mathbf{r}, t)$ originates from the source and travels through the subsurface region, and the back-propagated wavefield $R(\mathbf{r}, t)$ is obtained by propagating the time-reversed recorded data from the receiver locations to the subsurface. After we record the source-side wavefield and the receiver-side wavefield, the zero-lag cross-correlation imaging condition (Claerbout, 1971) is applied to produce a subsurface structural image, which is:

$$I(\mathbf{r}) = \int_0^T [W(t) * L_{pha}^S(\mathbf{r}, t)][\bar{D}(t) * L_{pha}^R(\mathbf{r}, t)]dt, \quad (1)$$

where L_{pha}^S and L_{pha}^R are the propagation terms of the source-side wavefield and receiver-side wavefield, respectively, representing the phase accumulation effect caused by the wave propagation (i.e., the phase of the impulse response). $W(t)$ is the input source wavelet, and $\bar{D}(t)$ is the time-reversed data. The $*$ symbol denotes the convolution. The first and second terms in the brackets are the source- and receiver-side wavefield, respectively. For ease of explanation, the amplitude effect (i.e., the amplitude of the impulse response) brought by the propagation is omitted in equation (1). The standard imaging condition (1) is based on the wave propagation process within a lossless medium, as shown in Figure 1a.

If the subsurface medium is visco-acoustic, then the amplitude of the recorded data

is attenuated and the phase of the recorded data is distorted by the frequency dependent phase velocity due to the finite Q. The attenuated data is related to the regular lossless data by

$$D^A(t) = D(t) * L_{phd}(v, Q) * L_a(v, Q), \quad (2)$$

where $D(t)$ and $D^A(t)$ are the recorded data in the acoustic and the visco-acoustic media, respectively. $L_{phd}(v, Q)$ is the phase distortion caused by Q , and $L_a(v, Q)$ is the Q -related amplitude reduction that differs from the propagation-related effects, such as geometrical spreading, transmission loss, etc. Figure 1b shows a wave propagation process in a visco-acoustic medium. Applying the time reversal operator on equation (2) gives

$$\bar{D}^A(t) = D^A(T - t) = \bar{D}(t) * L_{phd}^{-1}(v, Q) * L_a(v, Q), \quad (3)$$

where $L_{phd}^{-1}(v, Q)$ is the inverse of the operator $L_{phd}(v, Q)$. Applying the standard imaging condition (1) to the attenuated data, we have the resulting image

$$\begin{aligned} I(\mathbf{r}) &= \int_0^T [W(t) * L_{pha}^S][\bar{D}^A(t) * L_{pha}^R]dt \\ &= \int_0^T [W(t) * L_{pha}^S][\bar{D}(t) * L_{phd}^{-1}(v, Q) * L_a(v, Q) * L_{pha}^R]dt. \end{aligned} \quad (4)$$

Comparing equation (4) with the image produced by the data without attenuation, as shown in equation (1), we note that the phase change and the amplitude decay are expected in the resulting image if the standard imaging condition is applied to the attenuated data, as shown in Figure 1c. The image produced by the conventional RTM with attenuated data will be shifted in depth and be distorted. In order to compensate these attenuation effects that deteriorate the image quality, we need to design a new imaging condition that boosts the wavefield amplitudes (i.e., reverse the amplitude reduction process represented by L_a) during the source-side and receiver-side propagation. Also, the dispersion relation must be kept the same as the attenuation process to cancel the phase change introduced in

the time-reversal process by L_{phd}^{-1} in equation (4). The imaging condition can be designed to properly compensate the amplitude and the phase for attenuated seismic data when the amplitude reduction term L_a and the phase change term L_{phd} are decomposed to the source- and receiver-side parts:

$$\begin{aligned} I^C(\mathbf{r}) &= \int_0^T [W(t) * L_{pha}^S * L_{phd}^S * (L_a^S)^{-1}] [\bar{D}^A(t) * L_{pha}^R * L_{phd}^R * (L_a^R)^{-1}] dt \\ &= \int_0^T [W(t) * L_{ph}^S * (L_a^S)^{-1}] [\bar{D}^A(t) * L_{ph}^R * (L_a^R)^{-1}] dt \end{aligned} \quad (5)$$

where the superscripts S and R denote the source- and receiver-side operators, respectively.

$L_{ph}^S = L_{pha}^S * L_{phd}^S$ denotes the total phase change accumulated in the source-side wave propagation, and the receiver-side phase change L_{ph}^R is defined similarly. $I^C(\mathbf{r})$ denotes the compensated imaging result. In this Q-compensated imaging condition (5), the amplitudes of the source- and receiver-side wavefield are both boosted during the migration process, while the attenuation related phase change of both source- and receiver-side wavefield are the same, yielding the same image as equation (1). We emphasize that it is critical to keep the dispersion relation the same in both the forward and backward propagation processes.

In other words, the amplitude compensation operator is L_a^{-1} but the phase compensation operator is L_{phd} instead of L_{phd}^{-1} . This fact lays down the main challenge of developing a finite-difference based Q-RTM algorithm. Figure 1d shows the concept of the new imaging condition. If the compensated imaging condition is applied successfully, the resulting image is expected to be identical or nearly identical to the one produced by the data without attenuation under a standard imaging condition.

[Figure 1]

Although we use the operators L_a and L_{phd} to describe the amplitude effect and the phase effect during the wave propagation, normally these two effects are coupled in a stan-

dard wave equation. An explicitly phase-amplitude effect decoupled wave equation based on fractional derivatives is given by a series of work recently (Zhu and Harris, 2014; Zhu et al., 2014; Sun et al., 2015b), which can only be implemented by a pseudo-spectral method. Because pseudo-spectral methods are not computationally efficient for large scale problems, and are parallelization-unfriendly (Hu et al., 2016). A method based on finite-difference or other local numerical differential operators is more preferable for the Q-RTM production.

Visco-acoustic wave equation by local differential operators

To develop a local numerical differential operator based method for the wave propagation simulation with Q compensation capability, we first investigated the generalized standard linear solid (GSLS) methods for Q attenuation process simulation. The τ -method by Blanch et al. (1995) is an efficient GSLS method for visco-acoustic wave propagation simulations, which produces a nearly constant Q with frequency (i.e., frequency independent Q) through the introduction of several memory variables and the corresponding partial differential equations:

$$\begin{aligned} \frac{\partial v}{\partial t} &= -\frac{1}{\rho} \nabla p \\ -\frac{\partial p}{\partial t} &= M_R(1 + L\tau) \nabla \cdot v + \sum_{l=1}^L r_l \\ \frac{\partial r_l}{\partial t} &= -\tau \frac{M_R}{\tau_{\sigma l}} \nabla \cdot v - \frac{1}{\tau_{\sigma l}} r_l, \end{aligned} \quad (6)$$

where p is the pressure, v is the particle velocity, M_R is the bulk modulus, ρ is the density, and L is the number of relaxation mechanisms. $\tau_{\sigma l}$ and $\tau_{\epsilon l}$ are the stress relaxation time and strain relaxation time of each relaxation mechanism, respectively. $\tau = \tau_{\epsilon l}/\tau_{\sigma l} - 1$ is a dimensionless parameter, and r_l are the memory variables of each relaxation mechanism. The memory variables are used to simplify the convolution terms in the GSLS model

(Carcione et al., 1988; Robertsson et al., 1994) and there is no fractional order derivatives in equation (6). Consequently, finite-difference methods can be employed for solving the GSLS governing equations, while the global operators for the fractional order derivative evaluation in the KCQ model (Kjartansson, 1979; Zhu et al., 2014) are avoided. According to Robertsson et al. (1994) and Blanch et al. (1995), under the assumption $\tau \ll 1$, which is practically justified, Q and the phase velocity in this method can be expressed as:

$$Q(\omega) = \frac{(1 + L\tau) - \sum_{l=1}^L \frac{\tau}{1+\omega^2\tau_{\sigma l}^2}}{\sum_{l=1}^L \frac{\omega\tau\tau_{\sigma l}}{1+\omega^2\tau_{\sigma l}^2}} \quad (7)$$

$$c_p(\omega) \approx c \left[(1 + L\tau) - \sum_{l=1}^L \frac{\tau}{1+\omega^2\tau_{\sigma l}^2} \right]^{1/2}.$$

where $c = \sqrt{M_R/\rho}$ is the relaxed phase velocity, which equals to the phase velocity in acoustic media. As shown in equation (7), both the Q value and the phase velocity are functions of frequency. With a limited number (here we use 5) of relaxation mechanisms and an optimized set of $\tau_{\sigma l}$ and τ , one is able to obtain a nearly constant Q over a predefined frequency range $[\omega_a \omega_b]$ (the solid line in Figure 2a). The distribution of $\tau_{\sigma l}$ is pre-defined. In this work, we use the strategy described in Blanch et al. (1995) to select $\tau_{\sigma l}$ to let $\omega_l = 1/\tau_{\sigma l}$ distribute logarithmically over a larger frequency range, i.e., $\omega_l \in [0.1\omega_a \ 10\omega_b]$. The parameter τ is determined by the corresponding constant Q value. We optimize the Q value following Blanch's work to obtain a table of τ . As shown in Figure 2b, the normalized analytical phase velocity dispersion relation (solid line) is very close to the experimental results (Robertsson et al., 1994). In τ -method, the attenuation effects, including both the phase change and the amplitude decay, are represented by the summation of the memory variables and the corresponding PDE introduced in equation (6), which can be updated directly using a finite-difference method. In contrast to the pseudo-spectral operator, finite-difference is a local numerical differential operator, leading to high computational efficiency,

especially for large scale problems.

Direct Q-compensation with τ -method

For the purpose of accuracy, we need to revert the sign of Q to obtain a negative Q while precisely controlling the dispersion relation to be the same as the Q-attenuation process. In other words, the phase velocity must remain the same as the solid line shown in Figure 2b but the amplitude needs to be boosted. To achieve this goal, in equation (6), replacing $\tau_{\sigma l}$ by $-\tau_{\sigma l}$, we obtain a new system of equations where the phase velocity dispersion relation is the same as equation (7), and the Q value has the same magnitude but opposite in sign to the Q value in equation (7). Unfortunately, this strategy turned out to be an impractical method because the modified wave equation is not stable (Xie et al., 2015). Severe instability was observed in the first few steps of the receiver-side back-propagation process with Q-compensation in our numerical experiments. Therefore, this negative $\tau_{\sigma l}$ -method for visco-acoustic wave propagation modeling cannot be directly applied to the Q-compensation.

Here, we implement an alternative strategy. Instead of flipping the sign of $\tau_{\sigma l}$, we change the sign of τ to be negative to avoid the stability issue. This Q-compensation strategy is the so-called negative τ -method, which is equivalent to the existing GSLS based Q-RTM methods (Causse and Ursin, 2000; Deng and McMechan, 2007, 2008; Guo et al., 2016). The wave equation is

$$\begin{aligned} \frac{\partial v}{\partial t} &= -\frac{1}{\rho} \nabla p \\ -\frac{\partial p}{\partial t} &= M_R(1 - L\tau) \nabla \cdot v + \sum_{l=1}^L r_l \\ \frac{\partial r_l}{\partial t} &= \tau \frac{M_R}{\tau_{\sigma l}} \nabla \cdot v - \frac{1}{\tau_{\sigma l}} r_l \end{aligned} \quad (8)$$

With the assumption $\tau \ll 1$, the Q value and the phase velocity can be derived as:

$$\begin{aligned} Q'(\omega) &\approx -\frac{1}{\sum_{l=1}^L \frac{\omega \tau \tau_{\sigma l}}{1 + \omega^2 \tau_{\sigma l}^2}} \\ c'_p(\omega) &\approx c \left[(1 - L\tau) + \sum_{l=1}^L \frac{\tau}{1 + \omega^2 \tau_{\sigma l}^2} \right]^{1/2}. \end{aligned} \quad (9)$$

The negative τ scheme yields a $Q'(\omega)$ whose absolute value is slightly smaller than the expected value as shown in Figure 2a. With the negative τ scheme, the instability problem is successfully avoided and the amplitude compensation is realized due to the negative Q. However, there are two remaining issues to be addressed. First, because of the discrepancy between the specified Q value and the modeled negative Q produced by the negative τ scheme, over-compensation is expected. The second issue, observed as a phase distortion problem, is difficult to solve. The compensation process described by equation (8) has a wrong phase velocity dispersion relation (shown as the dotted line in Figure 2b). The negative τ -method's phase velocity decreases with frequency, which is much lower than the actual phase velocity, and has an opposite trend, leading to an upward shift of the imaged structures and the severe phase distortion. Consequently, the migration images produced by equation (8) may contain wavelets with wrong polarities and it might be difficult to use these images for geological interpretation.

In this work, we develop a novel approach to reduce the dispersion relation discrepancy and we call this new method the multi-stage optimized Q compensation.

[Figure 2]

Multi-stage Optimized Q-compensation method

We propose a multi-stage optimization method to correct the dispersion relation of the negative τ -method. The strategy is to introduce some polynomial optimization terms into

the real part of complex modulus while keeping the imaginary part fixed, intending to design a frequency dependent phase velocity correction term to match the ideal velocity for Q-compensation. To achieve this goal, we first convert equation (8) to a second order PDE system as follows:

$$\begin{aligned}\frac{\partial^2 p}{\partial t^2} &= c^2(1 - L\tau)\nabla^2 p - \sum_{l=1}^L s_l \\ \frac{\partial s_l}{\partial t} &= -\frac{\tau}{\tau_{\sigma l}}c^2\nabla^2 p - \frac{1}{\tau_{\sigma l}}s_l,\end{aligned}\tag{10}$$

where $c = \sqrt{M_R/\rho}$ and s_l are the new memory variables. Then, we introduce the polynomial dispersion optimization terms into equation (10) to adjust the dispersion relation curve of the system:

$$\begin{aligned}\frac{\partial^2 p}{\partial t^2} &= (1 - L\tau)c^2\nabla^2 p + \left(\alpha + \beta\frac{\partial^2}{\partial t^2} + \gamma\frac{\partial^4}{\partial t^4}\right)c^2\nabla^2 p - \sum_{l=1}^L s_l \\ \frac{\partial s_l}{\partial t} &= -\frac{\tau}{\tau_{\sigma l}}c^2\nabla^2 p - \frac{1}{\tau_{\sigma l}}s_l,\end{aligned}\tag{11}$$

where α , $\beta\frac{\partial^2}{\partial t^2}$, and $\gamma\frac{\partial^4}{\partial t^4}$ are the first, second, and third stage dispersion optimization terms. We may use the optimization parameters α , β , γ to adjust the dispersion relation curve over a certain frequency range. The corresponding phase velocity and the Q value in a homogeneous medium are

$$\begin{aligned}Q(\omega)^{OP} &\approx -\frac{1 - L\tau + \sum_{l=1}^L \frac{\tau}{1+\omega^2\tau_{\sigma l}^2} + \alpha - \beta\omega^2 + \gamma\omega^4}{\sum_{l=1}^L \frac{\omega\tau\tau_{\sigma l}}{1+\omega^2\tau_{\sigma l}^2}} \\ c_p(\omega)^{OP} &\approx c \left[1 - L\tau + \sum_{l=1}^L \frac{\tau}{1 + \omega^2\tau_{\sigma l}^2} + \alpha - \beta\omega^2 + \gamma\omega^4 \right]^{1/2}\end{aligned}\tag{12}$$

Here, $c_p(\omega)^{OP}$ stands for the optimized velocity. Parameters α , β , and γ are obtained by solving the inverse problem, $\min \|c_p(\omega)^{OP} - c_p(\omega)\|_2^2$ in a predefined frequency range $[\omega_1, \omega_2]$. As shown in equation (12), the introduction of even order time derivatives does not add any terms to the imaginary part of complex velocity.

Here, α serves as the 1-stage optimization parameter to shift the dispersion curve downward or upward without modifying the curve shape, as shown in Figure 3b; β serves as the 2-stage optimization parameter to modify the curvature of the dispersion curve as shown in Figure 3c; and γ is the 3-stage optimization term, which gives more degrees of freedom to fine tune the shape of the curve as plotted in Figure 3d. As illustrated by Figure 3, the phase velocity with 3 stages of optimization is more accurate and matches the targeted phase velocity curve very well in the frequency range of interest (10-70 Hz).

[Figure 3]

The dispersion optimization parameters are only dependent on Q , implying that the values of α , β , and γ can be pre-calculated and stored in a lookup table. Therefore, this is just a one-time computation and no extra cost is needed in the Q-RTM process. In most cases, 2-stage optimization scheme is accurate enough for the Q-compensation in RTM. The comparison between the Q values before and after the dispersion optimization is plotted in Figure 4.

[Figure 4]

Because equation (11) has no fractional order derivatives, the multi-stage optimized Q compensation can be implemented using local differential operators, such as a finite-difference method. Extra memory use incurred by the high order temporal derivatives in the optimization terms ($\alpha + \beta \frac{\partial^2 t}{\partial t^2} + \gamma \frac{\partial^4 t}{\partial t^4}$) in equation (11) can be avoided under the

approximation of $\tau \ll 1$ by converting them to the spatial derivatives as follows:

$$\begin{aligned}\frac{\partial^2 p}{\partial t^2} &= (1 - L\tau)c^2 \nabla^2(p + p^C) - \sum_{l=1}^L s_l \\ \frac{\partial s_l}{\partial t} &= -\frac{\tau}{\tau_{\sigma l}} c^2 \nabla^2 p - \frac{1}{\tau_{\sigma l}} s_l \\ p^C &= \alpha p + \beta c^2 \nabla^2 p + \gamma c^2 \nabla^2(c^2 \nabla^2 p)\end{aligned}\quad (13)$$

The detailed derivation of equation (13) is demonstrated in appendix A. Equation (13) is an easier form of the multi-stage Q optimization wave equation for implementation. Although some approximations are made to transform the time derivatives to the spatial derivatives, less than 0.5% extra numerical error is introduced according to our numerical test. If a 2-stage optimization is applied, equation (13) is a 2nd order PDE system, if a 3-stage optimization is applied, equation (13) is a 4th order PDE system.

NUMERICAL IMPLEMENTATION AND EXAMPLES

Validation of multi-stage optimized Q compensation

We employ a finite-difference method to implement the multi-stage optimized Q compensation. The scheme has the same stability criteria as the original τ -method in the Q attenuation modeling (Robertsson et al., 1994), i.e., $c_{max}\Delta t / \min(\Delta x, \Delta y, \Delta z) < 1$, where $c_{max} = \sqrt{(1 + L\tau)M_R/\rho}$ is the unrelaxed phase velocity of GSLS viscoacoustic model. We apply a low-pass filter during the back-propagation to prevent the high frequency noise from growing exponentially. To investigate our Q-compensation method's performance on the wavelet shape recovery, a 1D numerical test is conducted. The Q and velocity models are homogeneous with $Q = 40$ and $c_p = 2500$ m/s, respectively. As shown in Figure 5, we first propagate a Ricker wavelet with a dominant frequency of 30 Hz (Figure 5a) in this medium to record the attenuated data at the receiver located 1500 m away from the source (Figure

5b). Next, we input the time-reversed data at the receiver location, and back-propagate it with the multi-stage optimized Q-compensation algorithm. The compensated data is recorded at the source location (Figure 5c). As shown in Figure 5c, the compensated back-propagated data is very similar to the Ricker wavelet. The waveform is nearly symmetric and the amplitude is close to the acoustic back-propagation result using the unattenuated data at the same offset (Figure 5a). The slightly earlier arrival of high frequency components observed in Figure 5c is due to the imperfect dispersion relation optimization results. However, this dispersion relation error is controlled within the acceptable tolerance. For comparison, Figure 5d shows the Q-compensated result using the negative τ -method without dispersion optimization. We note that the waveform is severely distorted due to the wrong dispersion relation. As shown in Figures 5e and 5f, both the amplitude spectrum and the phase spectrum of the back propagated data with the multi-stage Q-compensation (dashed lines) are nearly identical to the spectra of the input Ricker wavelet (dotted lines), while the attenuated data suffers from the loss of high frequency components, severely reduced amplitude, and distorted phase (dotted line in Figure 5e and 5f). Accordingly, our new method can restore the lost high frequency components and the distorted phase caused by the Q-related attenuation effect.

[Figure 5]

Another numerical test is conducted to validate the numerical accuracy of the finite-difference implementation. In this 2D test with a constant Q of 60 and a homogeneous velocity of 1700 m/s, the two receivers are deployed 1500 m and 1510 m away from the source respectively. We used an 8th order finite-difference scheme with the grid space of 2.5

m. The numerical velocity and the numerical attenuation coefficient can be measured by

$$c(\omega) = \frac{\omega d}{\phi_1 - \phi_2}, \quad a(\omega) = \frac{1}{d} \ln \frac{A_2}{A_1}, \quad (14)$$

where A_i, ϕ_i are the amplitude and phase of the i th receiver, and d is the offset between the two receivers. The theoretical attenuation coefficient for compensation process $a(\omega)$ is defined from the solution of the wave equation

$$u = Ae^{i\omega t - ikx} e^{a(\omega)x}, \quad a(\omega) = \frac{\omega}{2Qc(\omega)}. \quad (15)$$

Here, the attenuation coefficient is positive, indicating the method boosts the amplitude. Figure 6 shows the measured numerical dispersion curve and the numerical attenuation coefficient in comparison with the theoretical dispersion curve and the attenuation coefficient, respectively. The numerical experiment results are in good agreement with the theoretical curves.

[Figure 6]

Numerical examples of Q-RTM

We present a simple layered model first to show the Q-compensation performance, and then a more complex model, to further demonstrate the capability of this Q-RTM method.

[Figure 7]

Figure 7 shows the result of a 3-layer model RTM. The size of the computational domain is 1600 m by 1600 m with the grid spacing of 4 m. The velocities and Q values of each layer are shown in Figure 7d. We input a Ricker wavelet with the dominant frequency of 30 Hz. Figure 7a is the conventional RTM image (i.e., without Q-compensation) using unattenuated data, which serves as the reference solution. Figure 7b is the Q-RTM image produced by the

multi-stage Q-compensation method with the attenuated data, and Figure 7c is the image generated by a conventional RTM method (i.e., without compensation) with the attenuated data. As shown in the figures, the image produced by the conventional method has dim and depth-shifted structures. Our multi-stage optimized Q-RTM method boosts the amplitude and the structure depths are imaged correctly. According to Figure 7e, this Q-RTM result is nearly identical to the reference. Guo et al. (2016) reported that images produced by the direct GSLS method show severely distorted wiggles and the upward-shifted migration depth compared to the reference, even though the image amplitudes are recovered. Figure 7 demonstrates that this Q-RTM algorithm has successfully eliminated these problems by introducing the multi-stage optimization technique.

We tested the Q-RTM algorithm on a more realistic synthetic example, the Sigsbee 2A model. The velocity model is shown in Figure 8a, and the Q model is shown in Figure 8b. We set the minimum Q to be 40 in the two main attenuation anomalies. The input is a Ricker wavelet with the dominant frequency of 20 Hz. We use an $O(2,16)$ finite-difference scheme for the simulation. The NPML (Hu and Cummer, 2004; Hu et al., 2007) absorbing boundary condition is applied to eliminate the artificial reflections from the boundaries. All the shots and receivers are deployed at $z=100$ m. Figures 8c-8f are the conventional RTM result using the attenuated data, the multi-stage optimized Q-RTM result using the attenuated data, the conventional RTM result using the unattenuated data, and the pseudo-spectral based Q-RTM using the attenuated data (Zhu et al., 2014), respectively. As shown in Figure 8c, the conventional RTM suffers from the resolution reduction below the Q anomalies. Compared to Figures 8c and 8e, the image quality of our result shown in Figure 8d is significantly improved with both the amplitude and the phase accurately compensated and the geological details reconstructed properly. The structure depths are more accurate and match with the

reference solution as expected. Figures 8g and 8h show a trace comparison and its spectrum analysis. The vertical trace is selected at $x = 2187.5$ m, below the biggest low-Q anomaly. This numerical example validated that the local operator based Q-RTM algorithm has the capability of compensating the amplitude and phase simultaneously without sacrificing the accuracy.

[Figure 8]

DISCUSSION

Combining the negative τ scheme and the multi-stage dispersion optimization technique, our Q-compensation method can recover the degraded images over the frequency range of 10-70 Hz accurately but loses its accuracy below 10 Hz. According to Figures 3c, 3d and 4c, 4d, the Q value error between 10 Hz and 70 Hz is controlled within 2%, while the normalized phase velocity dispersion curve variation is within 1%. The dispersion error below 10 Hz causes some artifacts. Some low-level waveform distortion and phase shift are observed in the compensation result due to the imperfect match between the optimized phase velocity dispersion and the ideal phase velocity dispersion. The phase shift is linearly proportional to the phase velocity optimization error, which is about 0.2-0.5% (for 2- and 3-stage optimization, respectively) according to our numerical tests. Currently, we are investigating some alternative strategies for the dispersion relation optimization at the low frequency regime, which will be reported separately in another paper. If the low frequency error is reduced, this method will not only be suitable for Q-RTM, but also be applicable for Q-FWI, a full waveform inversion method that attempts to invert both velocity model and Q model.

The optimization parameters α , β , and γ , along with the compensation parameter τ , are pre-computed in the method. All of the parameters are determined through an optimization procedure over the specified frequency band and the Q range. These parameters are independent of the seismic velocity, which means we can set up a general lookup table storing these parameters to avoid the recalculation of these parameters within the Q-RTM engine. According to the analytical dispersion relation analysis result shown in Figure 3c and 3d, both the 2- and 3-stage optimization schemes provide the phase velocities close to the ideal one. On the other hand, the 1-stage dispersion optimization scheme may correct the migration depth but it is expected to result in severe wavelet distortion due to the large dispersion error shown in Figure 3b. Theoretically, the 3-stage optimization scheme is more accurate than the 2-stage scheme. A 4-stage optimization scheme, which is more computationally expensive, further reduces the dispersion error, but it has a risk of a stability issue. To balance the computational cost, the algorithm stability, and the migration image quality, we recommend to use the 2-stage optimization method for most applications. However, for cases where the Q effect is very strong (e.g., $Q < 20$, propagation distance > 3 km, dominant frequency > 30 Hz), the 3-stage scheme needs to be employed to minimize the negative impact brought by accumulating the phase error.

Similar to most existing Q migration algorithms, the finite-difference based Q-RTM method has the same stability issue if the recorded data contain high frequency noise. In order to suppress exponentially growing high frequency noise in the Q compensation procedure, we apply a finite impulse response filter (FIR) to the wave propagation engine. The FIR filter is designed by the frequency sampling method combined with a Kaiser Window technique. The filter is only applied to the dispersion optimization term p^C and the memory variables s_l . According to the numerical experiments, this filtering procedure

effectively mitigates the stability issue. To make this Q-compensation algorithm GPU friendly, the width of the Kaiser Window function for the FIR is tightly controlled without violating its frequency response specifications.

Compared with the pseudo-spectral based Q-RTM, the finite-difference based Q-RTM uses shorter stencils for the spatial derivative computation and is more suitable for domain decomposition. Hence, for large scale problems, it is more computationally efficient and saves memory substantially. The FFT with n-grid trace has computational complexity of $O(n * \log_2 n)$, while the computational complexity of finite difference method is $O(n * m)$, where m is the spatial order of accuracy. Thus the computational cost of the finite difference method grows linearly, which is slower than the pseduo-spectral method. If $m < \log_2 n$, the finite difference method has the advantage of computational cost. On the other hand, our multi-stage optimized Q-RTM uses local differential operators, which makes it very suitable for a domain decomposition strategy, thus converting large size problems to multiple smaller size problems to fit in parallel computation with a manageable amount of information exchange. Global operators are naturally unfriendly to domain decomposition and parallel computing. Although there are some parallel Fourier pseudo-spectral algorithms (Pelz, 1991; Yin et al., 2005) for solving partial differential equations in large 3D circumstances (Ayala and Wang, 2013), such parallel algorithms rely on complex domain decomposition strategies and require extensive memory use and many communications between computational nodes. Recently, GPU computing has been widely used in the oil/gas industry for the RTM acceleration (Abdelkhalek et al., 2009). Due to the large temporary memory usage associated with global operators, pseudo-spectral methods are not suitable for GPU implementation because the shared memory on a GPU is often too small to accommodate the whole computational domain required by the pseudo-spectral methods. The multi-stage

optimized Q-RTM, has shown its advantages in a GPU implementation because of its short stencil. Furthermore, this multi-stage optimization algorithm can be easily incorporated into the currently existing RTM production code with minimum effort.

CONCLUSION

The newly developed multi-stage optimized Q-compensation method has the accurate amplitude and phase reconstruction capability. It successfully improves the quality of earth imaging when there are visco-acoustic overburdens in presence. Although this algorithm is less accurate for low frequency components, over the frequency range of (10 - 70 Hz), it performs properly in both simple and complex geological settings. The main advantage of this method is its computational efficiency, limited memory usage, and suitability for parallel computing and GPU implementation, compared with the existing pseudo-spectral Q-RTM methods, especially for large scale 3D production. The main challenge in the development of this method is to compensate the phase and amplitude simultaneously and accurately during the back-propagation process. The difficulty is overcome by combining the negative τ scheme and the multi-stage polynomial optimization algorithm. The negative τ scheme boosts the amplitude without losing the stability, while the multi-stage polynomial optimization method reverts the phase distortion in the recorded attenuated seismic data. Similar to most Q-RTM algorithms, a low-pass FIR filter needs to be applied to prevent the stability issue caused by high frequency noises. Synthetic examples validate this Q-RTM method and demonstrate its performance in complex geological structures. In conclusion, this novel multi-stage optimized Q-RTM algorithm can compensate both the amplitude and the phase with high accuracy, producing high quality images nearly identical to the Q-RTM methods based on pseudo-spectral operators, and significantly saving the computational

cost and turnaround time.

ACKNOWLEDGMENTS

We thank AGT for supporting this study. The work of TZ and JN was also partially supported by the Special Fund for Earthquake Research in Public Interest under Grant 201408013. We are also appreciate to the assistant editor Dr. John Etgen, the associate editor Dr. Jonas D. De Basabe, Dr. Junze Sun and all three anonymous reviewers for their effort and valuable suggestions that are greatly helpful for us to improve the manuscript.

APPENDIX A

CONVERSION OF TIME DERIVATIVE TO SPATIAL DERIVATIVE

After the optimization parameters α , β , and γ are obtained, equation (11) is ready to be discretized. However, from the memory and computation efficiency perspective, high order time derivative evaluation is not preferable for numerical implementation. In this work, we propose a strategy to convert the time derivatives in equation (11) to the spatial derivatives without sacrificing the numerical accuracy. The first formulation of equation (11) can be written in the frequency domain

$$(i\omega)^2 p = (1 - L\tau)c^2 \nabla^2 p + (\alpha - \beta\omega^2 + \gamma\omega^4)c^2 \nabla^2 p - \sum_{l=1}^L s_l \quad (\text{A-1})$$

where

$$s_l = -\frac{\tau}{1 + i\omega\tau_\sigma} c^2 \nabla^2 p \quad (\text{A-2})$$

Observing the right-hand-side of equation (A-1), we note that $-L\tau + \alpha - \beta\omega^2 + \gamma\omega^4 \ll 1$, thus equation (A-1) can be approximated by

$$(i\omega)^2 p = c^2 \nabla^2 p - \sum_{l=1}^L s_l. \quad (\text{A-3})$$

For example, with the parameter setting being $Q = 60$, $\tau = 0.0188$, $\alpha = 0.0933$, $\beta = -4.18 \times 10^{-7}$, and $\gamma = -1.21 \times 10^{-12}$, the values of $-L\tau + \alpha - \beta\omega^2 + \gamma\omega^4$ at 10 Hz, 30 Hz, and 70 Hz are 9.313×10^{-4} , 0.0126, and 0.0349, respectively, which justifies the approximation made in equation (A-3). Furthermore, because $\tau \ll 1$, equation (A-2) suggests that the second term on the right-hand-side of equation (A-3) can be dropped without degrading the accuracy significantly, further reducing equation (A-3) to

$$\frac{\partial^2 p}{\partial t^2} = c^2 \nabla^2 p. \quad (\text{A-4})$$

Substituting equation (A-4) into equation (11), we have

$$\frac{\partial^2 p}{\partial t^2} = (1 - L\tau)c^2 \nabla^2(p + p^C) - \sum_{l=1}^L s_l \quad (\text{A-5})$$

where

$$p^C = \alpha p + \beta c^2 \nabla^2 p + \gamma c^2 \nabla^2(c^2 \nabla^2 p) \quad (\text{A-6})$$

and the α , β , and γ are scaled by $1/(1 - L\tau)$. The error analysis has been conducted and the analysis results indicate that the phase velocity error introduced by the above approximation is approximately 0.1%.

REFERENCES

- Abdelkhalek, R., H. Calandra, O. Coulaud, J. Roman, and G. Latu, 2009, Fast seismic modeling and reverse time migration on a GPU cluster: 2009 International Conference on High Performance Computing Simulation, 36–43.
- Abubakar, A., W. Hu, P. M. V. D. Berg, and T. M. Habashy, 2008, A finite-difference contrast source inversion method: *Inverse Problems*, **24**, 065004.
- Abubakar, A., W. Hu, T. M. Habashy, and P. M. Van, den Berg, 2009, Application of the finite-difference contrast-source inversion algorithm to seismic full-waveform data: *Geophysics*, **74**, WCC47–WCC58.
- Abubakar, A., G. Pan, M. Li, L. Zhang, T. M. Habashy, and P. M. V. D. Berg, 2011, Three-dimensional seismic full-waveform inversion using the finite-difference contrast source inversion method: *Geophysical Prospecting*, **59**, 874–888.
- Ayala, O., and L. P. Wang, 2013, Parallel implementation and scalability analysis of 3D fast fourier transform using 2D domain decomposition: *Parallel Computing*, **39**, 58–77.
- Bai, J., G. Chen, D. Yingst, and J. Leveille, 2013, Attenuation compensation in viscoacoustic reverse time migration, *in* SEG Technical Program Expanded Abstracts 2013: Society of Exploration Geophysicists, 3825–3830.
- Baysal, E., D. K. Dan, and J. W. C. Sherwood, 1983, Reverse time migration: *Geophysics*, **48**, 1514–1524.
- Bickel, S. H., and R. R. Natarajan, 1985, Plane-wave Q deconvolution: *Geophysics*, **50**, 1426–1439.
- Blanch, J. O., J. O. A. Robertsson, and W. W. Symes, 1995, Modeling of a constant Q: Methodology and algorithm for an efficient and optimally inexpensive viscoelastic technique: *Geophysics*, **60**, 176–184.

- Carcione, J. M., D. Kosloff, and R. Kosloff, 1988, Wave propagation simulation in a linear viscoacoustic medium: *Geophysical Journal International*, **93**, 393–401.
- Causse, E., and B. Ursin, 2000, Viscoacoustic reverse-time migration: *Journal of Seismic Exploration*, **9**, 165–184.
- Cavalca, M., I. Moore, L. Zhang, S. L. Ng, R. Fletcher, and M. Bayly, 2011, Ray-based tomography for Q estimation and Q compensation in complex media: *SEG Technical Program Expanded Abstracts 2011*, Society of Exploration Geophysicists, 3989–3993.
- Claerbout, J. F., 1971, Toward a unified theory of reflector mapping: *Geophysics*, **36**, 467–481.
- Clark, R. A., P. M. Benson, A. J. Carter, and C. A. G. Moreno, 2009, Anisotropic P-wave attenuation measured from a multi-azimuth surface seismic reflection survey: *Geophysical Prospecting*, **57**, 835–845.
- Dai, N., and G. F. West, 1994, Inverse Q migration: *SEG Technical Program Expanded Abstracts 1994*, Society of Exploration Geophysicists, 1418–1421.
- Dai, W., Z. Xu, and R. Coates, 2015, Least-squares reverse-time migration for visco-acoustic media, *in SEG Technical Program Expanded Abstracts 2015*: Society of Exploration Geophysicists, 3387–3391.
- Deng, and McMechan, 2007, True-amplitude prestack depth migration: *Geophysics*, **72**, S155–S166.
- Deng, F., and A. McMechan, George, 2008, Viscoelastic true-amplitude prestack reverse-time depth migration: *Geophysics*, **73**, S143–S155.
- Dutta, G., 2016, Skeletonized wave-equation inversion for Q, *in SEG Technical Program Expanded Abstracts 2016*: Society of Exploration Geophysicists, 3618–3623.
- Dutta, G., and G. T. Schuster, 2014, Attenuation compensation for least-squares reverse

- time migration using the viscoacoustic-wave equation: *Geophysics*, **79**, S251–S262.
- , 2016, Wave-equation Q tomography: *Geophysics*, **81**, R471–R484.
- Etgen, J., S. H. Gray, and Y. Zhang, 2009, An overview of depth imaging in exploration geophysics: *Geophysics*, **74**, WCA5–WCA17.
- Guo, P., G. A. Mcmechan, and H. Guan, 2016, Comparison of two viscoacoustic propagators for Q-compensated reverse time migration: *Geophysics*, **81**, S281–S297.
- Hargreaves, N. D., 1991, Inverse Q filtering by fourier transform: *Geophysics*, **56**, 519–527.
- Hu, W., A. Abubakar, and T. Habashy, 2007, Application of the nearly perfectly matched layer in acoustic wave modeling: *Geophysics*, **72**, SM169–SM175.
- Hu, W., and S. A. Cummer, 2004, The nearly perfectly matched layer is a perfectly matched layer: *IEEE Antennas and Wireless Propagation Letters*, **3**, 137–140.
- Hu, W., J. Liu, L. Bear, and C. Marcinkovich, 2011, A robust and accurate seismic attenuation tomography algorithm: SEG Technical Program Expanded Abstracts 2011, Society of Exploration Geophysicists, 2727–2731.
- Hu, W., T. Zhou, and J. Ning, 2016, An efficient Q-RTM algorithm based on local differentiation operators: SEG Technical Program Expanded Abstracts 2016, Society of Exploration Geophysicists, 4183–4187.
- Kjartansson, E., 1979, Constant Q- wave propagation and attenuation: *Journal of Geophysical Research Solid Earth*, **84**, 4737–4748.
- Li, M. K., C. C. Weng, and L. J. Jiang, 2006, A domain decomposition scheme based on equivalence theorem: *Microwave and Optical Technology Letters*, **48**, 1853–1857.
- Muller, T. M., B. Gurevich, and M. Lebedev, 2010, Seismic wave attenuation and dispersion resulting from wave-induced flow in porous rocks - a review: *Geophysics*, **75**, 75A147–75A164.

- Pelz, R. B., 1991, The parallel fourier pseudospectral method: *Journal of Computational Physics*, **92**, 296–312.
- Robertsson, J. O., J. O. Blanch, and W. W. Symes, 1994, Viscoelastic finite-difference modeling: *Geophysics*, **59**, 1444–1456.
- Shen, Y., B. Biondi, R. Clapp, and D. Nichols, 2014, Wave-equation migration Q analysis (WEMQA), *in* SEG Technical Program Expanded Abstracts 2014: Society of Exploration Geophysicists, 3757–3762.
- Shen, Y., and T. Zhu, 2015, Image-based Q tomography using reverse time Q migration, *in* SEG Technical Program Expanded Abstracts 2015: Society of Exploration Geophysicists, 3694–3698.
- Sun, J., S. Fomel, and T. Zhu, 2015a, Preconditioning least-squares RTM in viscoacoustic media by Q-compensated RTM, *in* SEG Technical Program Expanded Abstracts 2015: Society of Exploration Geophysicists, 3959–3965.
- Sun, J., S. Fomel, T. Zhu, and J. Hu, 2016, Q-compensated least-squares reverse time migration using low-rank one-step wave extrapolation: *Geophysics*, **81**, S271–S279.
- Sun, J., T. Zhu, and S. Fomel, 2015b, Viscoacoustic modeling and imaging using low-rank approximation: *Geophysics*, **80**, A103–A108.
- Traynin, P., J. Liu, and J. M. Reilly, 2008, Amplitude and bandwidth recovery beneath gas zones using kirchhoff prestack depth Q-migration: *SEG Technical Program Expanded Abstracts*, Society of Exploration Geophysicists, 2412–2416.
- Xie, Y., J. Sun, Y. Zhang, and J. Zhou, 2015, Compensating for visco-acoustic effects in TTI reverse time migration: *SEG Technical Program Expanded Abstracts 2015*, Society of Exploration Geophysicists, 3996–4001.
- Xin, K., B. Hung, K. X. Cggveritas, and B. H. Cggveritas, 2010, 3D Q tomography for com-

pensating frequency dependent attenuation and dispersion: Presented at the 72nd EAGE Conference and Exhibition incorporating SPE EUROPEC 2010, European Association of Geophysicists and Engineers.

Yin, Z., L. Yuan, and T. Tang, 2005, A new parallel strategy for two-dimensional incompressible flow simulations using pseudo-spectral methods: *Journal of Computational Physics*, **210**, 325–341.

Yu, Y., R. S. Lu, and M. M. Deal, 2002, Compensation for the effects of shallow gas attenuation with viscoacoustic wave equation migration: *SEG Technical Program Expanded Abstracts 2002*, Society of Exploration Geophysicists, 2062–2065.

Zhang, Y., P. Zhang, and H. Zhang, 2010, Compensating for visco-acoustic effects in reverse-time migration: *SEG Technical Program Expanded Abstracts 2010*, Society of Exploration Geophysicists, 3160–3164.

Zhou, J., S. Birdus, B. Hung, T. Keat, Huat, X. Yi, C. Dimitri, C. Amy, and W. Darrell, 2011, Compensating attenuation due to shallow gas through Q tomography and Q-PSDM, a case study in brazil: *SEG Technical Program Expanded Abstracts 2011*, Society of Exploration Geophysicists, 3332–3336.

Zhu, T., and J. M. Harris, 2014, Modeling acoustic wave propagation in heterogeneous attenuating media using decoupled fractional laplacians: *Geophysics*, **79**, T105–T116.

Zhu, T., J. M. Harris, and B. Biondi, 2014, Q-compensated reverse-time migration: *Geophysics*, **79**, S77–S87.

FIGURES

FigureList: (Total: 8)

Figure 1: Theory of RTM and Q-RTM

Figure 2: Q value and phase velocity of τ -method and direct negative τ -method

Figure 3: Phase velocity recovery under the multi-stage Q- optimization method ($Q = 60$)

Figure 4: Q value recovery under the multi-stage Q- optimization method ($Q = 60$)

Figure 5: Wavelet compensation under the multi-stage Q- optimization method ($Q = 40$)

Figure 6: Numerical accuracy of attenuation coefficient and phase velocity ($Q = 60$)

Figure 7: 3-layer Q-RTM numerical example

Figure 8: Sigsbee model Q-RTM numerical test

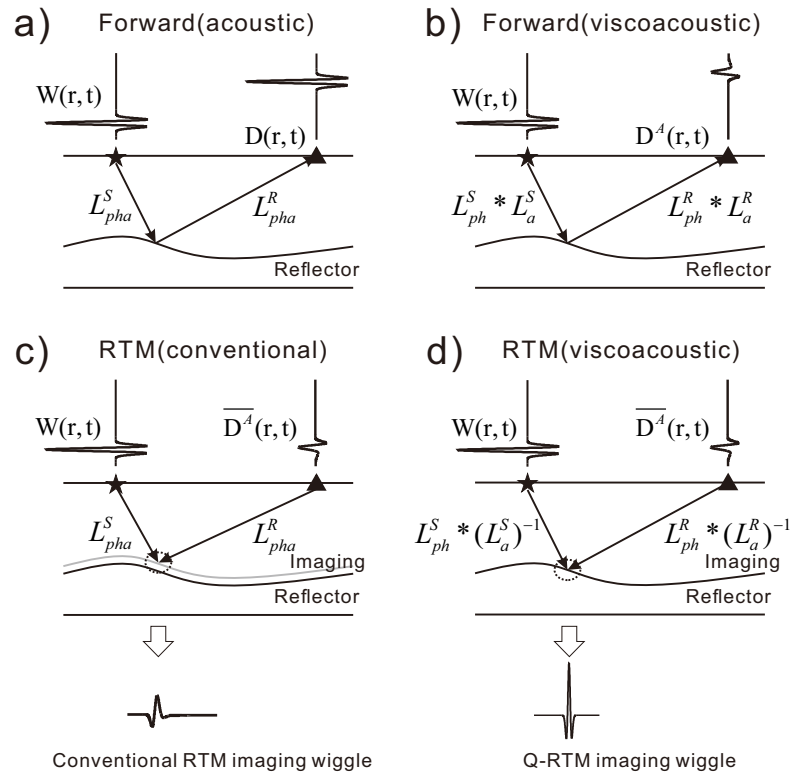


Figure 1: Theory of RTM and Q-RTM

a) acoustic forward propagation process; b) visco-acoustic forward propagation process; c) conventional RTM using attenuated data, the light grey image represents the dimming and shifted imaging result; d) Q-RTM using attenuated data.

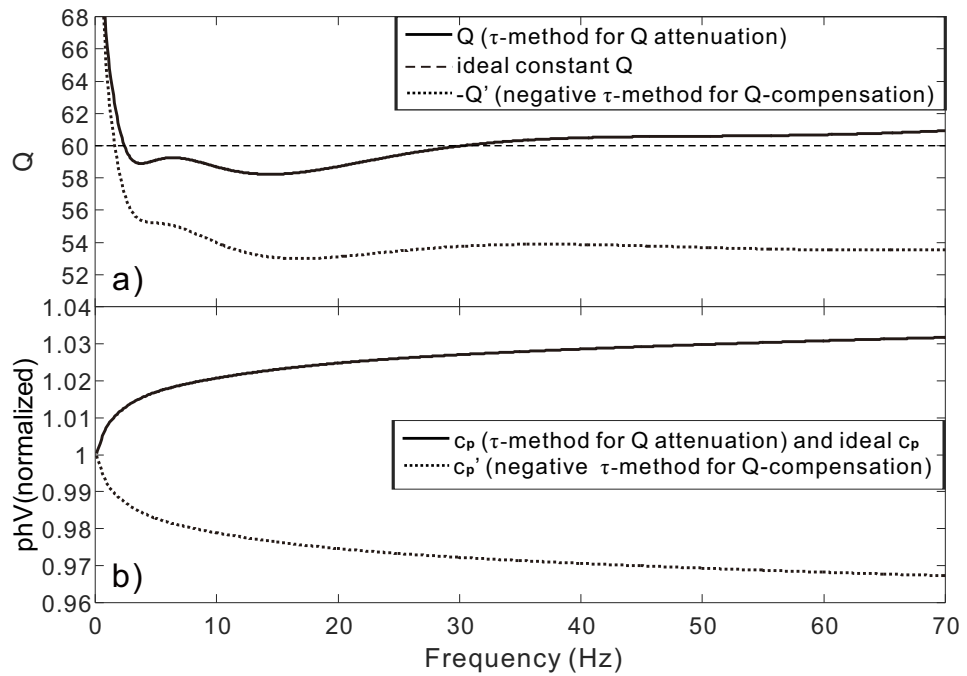


Figure 2: Q value and phase velocity of τ -method and direct negative τ -method

a) Q value; b) phase velocity; solid line represents Q-attenuation process, dotted line represents direct negative τ propagation process.

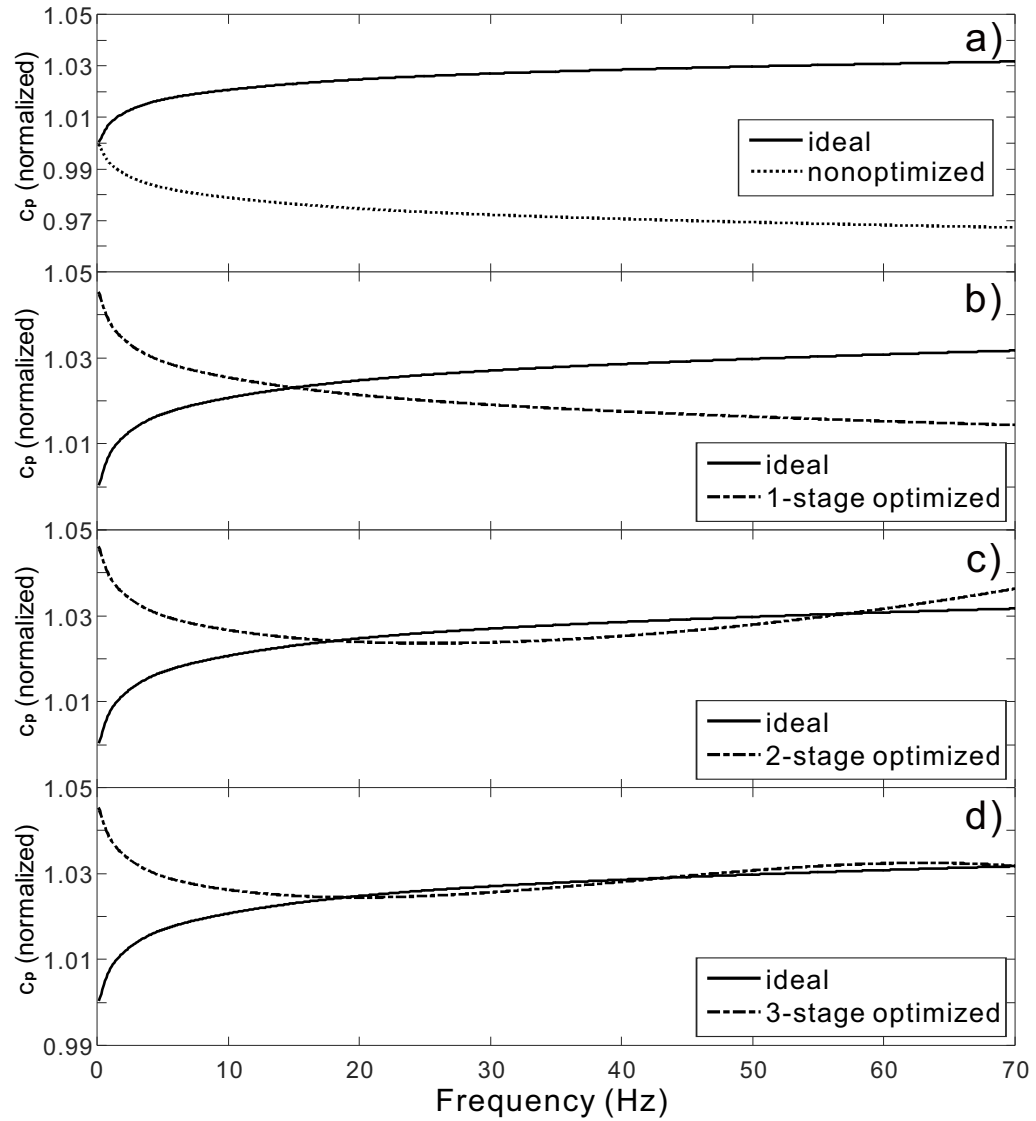


Figure 3: Phase velocity recovery under the multi-stage Q - optimization method ($Q = 60$)

a) non-optimized; b) 1-stage optimized; c) 2-stage optimized; d) 3-stage optimized.

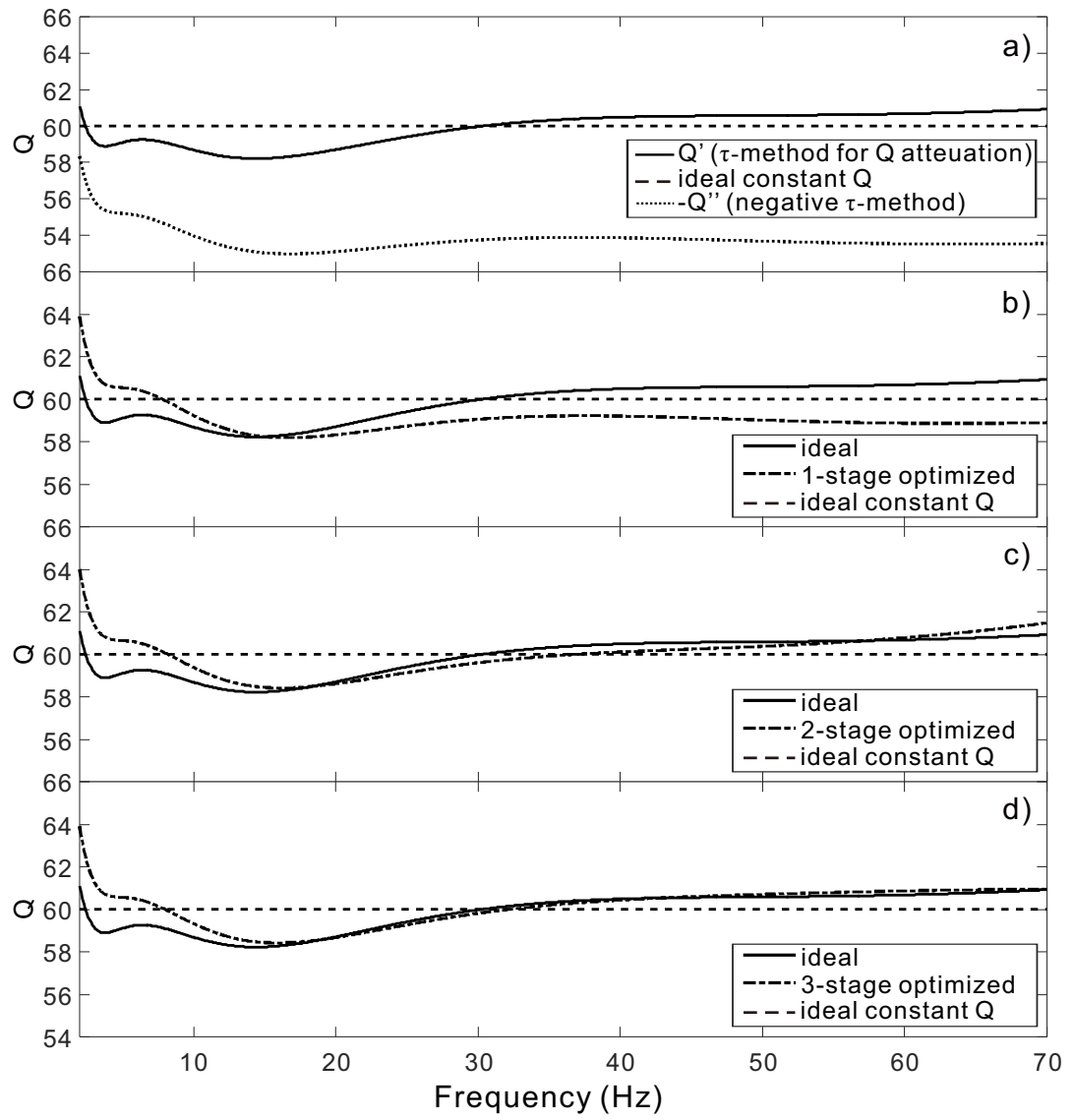


Figure 4: Q value recovery under the multi-stage Q - optimization method ($Q = 60$)

a) non-optimized; b) 1-stage optimized; c) 2-stage optimized; d) 3-stage optimized.

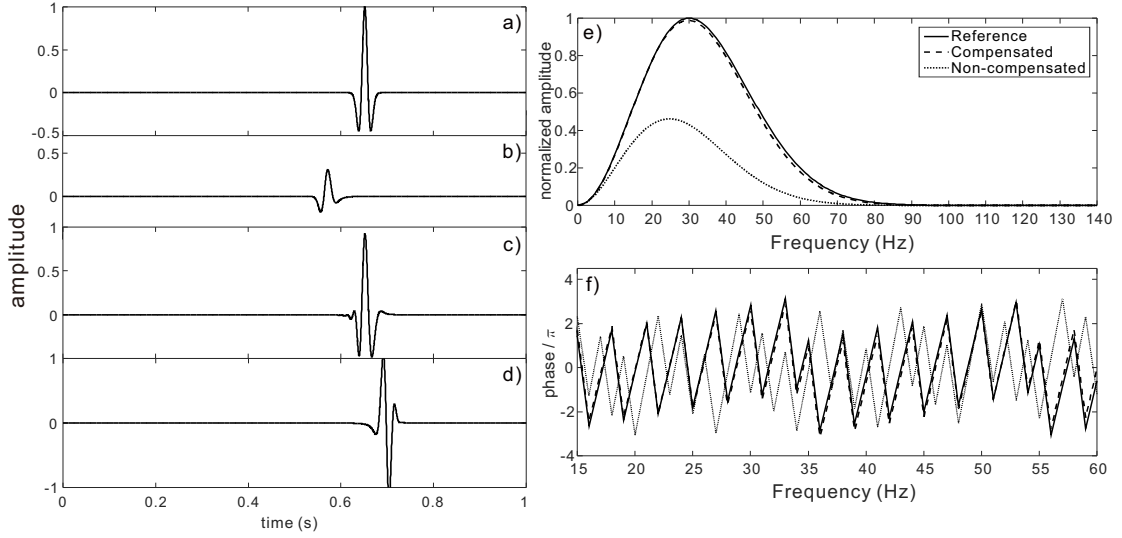


Figure 5: Wavelet compensation under the multi-stage Q- optimization method ($Q = 40$)

a) acoustic propagation process; b) Q-attenuation process; c) multi-stage optimized Q-compensation process; d) direct negative τ -method; e) amplitude spectrum; f) phase spectrum; In spectrum figures, solid line is reference, dashed line is multi-stage optimized Q-compensated spectrum, dotted line is Q-attenuated spectrum.

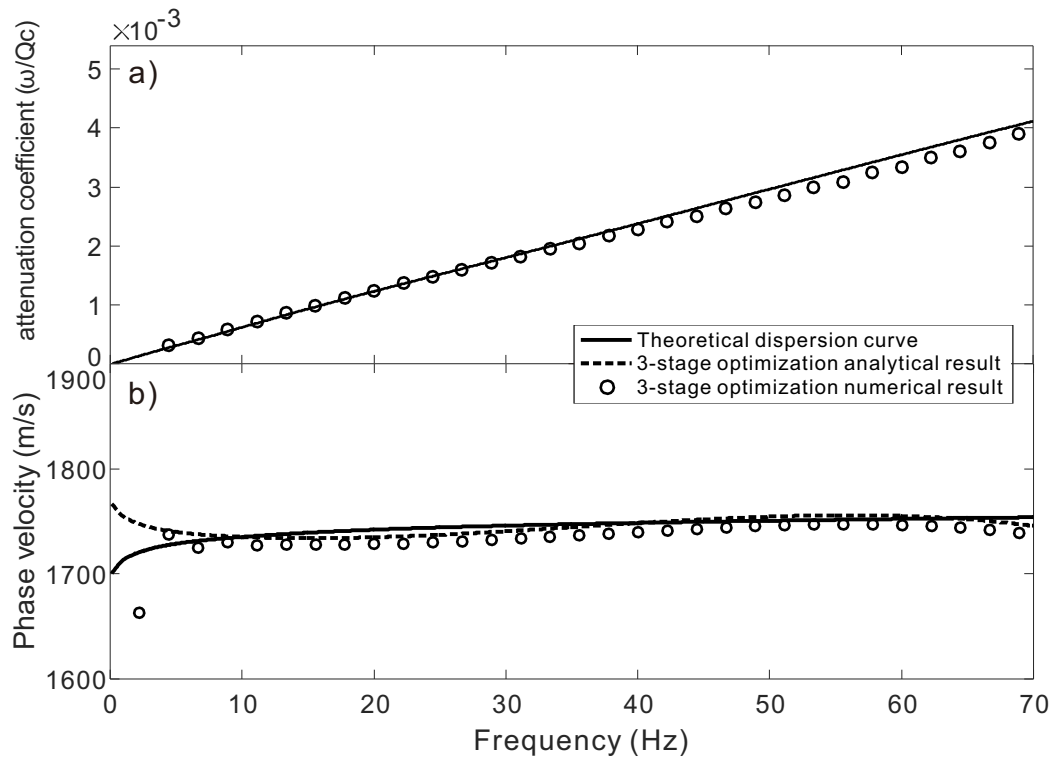


Figure 6: Numerical accuracy of attenuation coefficient and phase velocity ($Q = 60$)

a) attenuation coefficient; b) phase velocity.

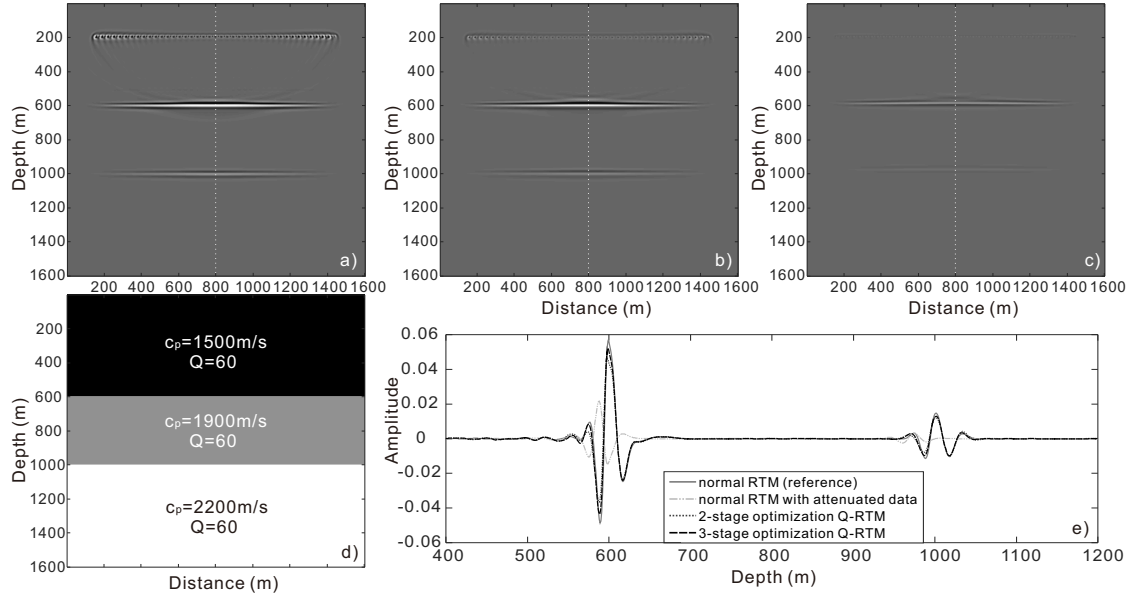


Figure 7: 3-layer Q-RTM numerical example

- a) normal RTM using the unattenuated data; b) multi-stage optimized Q-RTM using the attenuated data; c) conventional RTM using the attenuated data; d): velocity model; e): vertical section at the center, showing the wiggles along the white dashed line of a, b, and c.

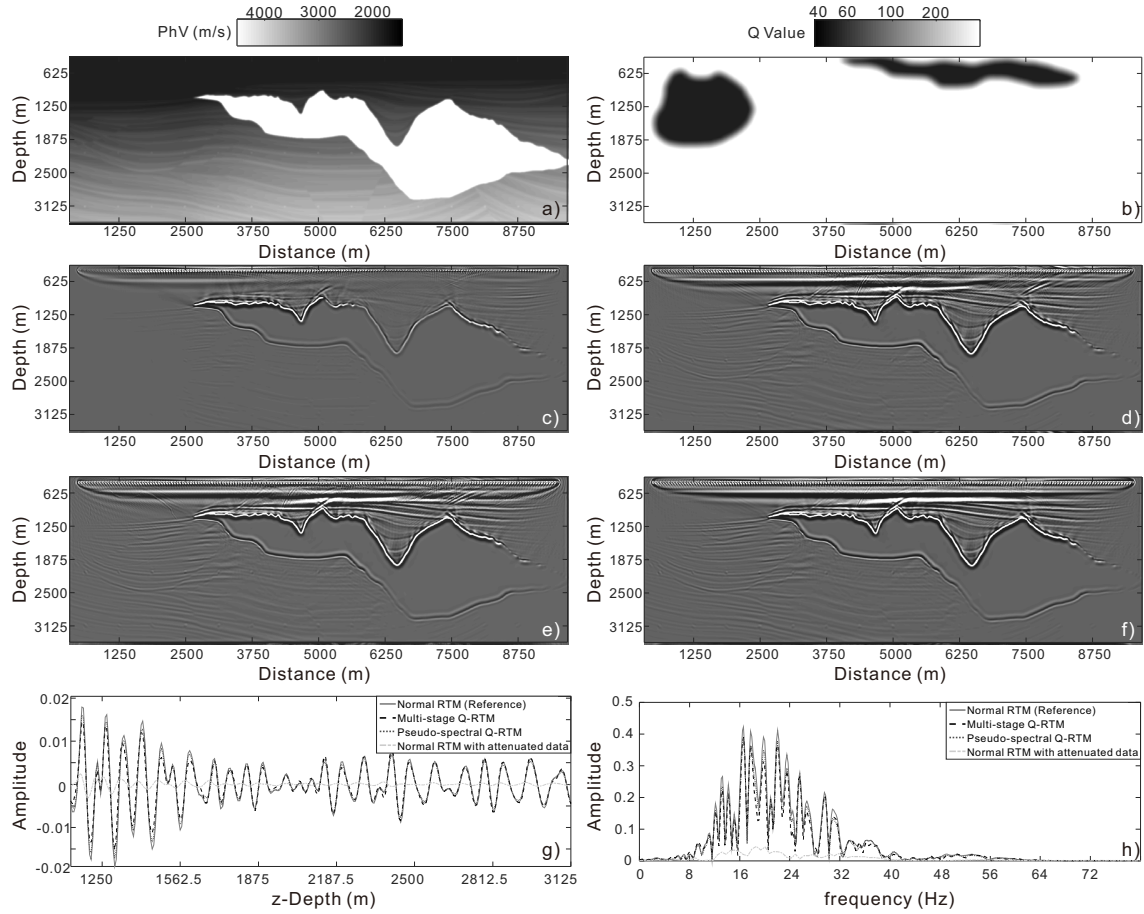


Figure 8: Sigsbee model Q-RTM numerical test

a) velocity model; b) Q model; c) conventional RTM using the attenuated data; d) multi-stage optimized Q-RTM using the attenuated data; e) pseudospectral Q-RTM; f) normal RTM using the unattenuated data; g) trace comparison of c f, at $x = 2187.5$ m; h) spectrum analysis of g).